Barrington, James H.; James, Stephen W.; Kissinger, Thomas; Staines, Stephen E.; Prince, Simon; Alcusa-Saez, Erica; Lawson, Nicholas J.; Tatam, Ralph P.

Optical fibre pressure sensing using a frequency modulated laser-based signal processing technique

Optical fibre pressure sensing using a frequency modulated laser-based signal processing technique

J H Barrington[1] , **S W James**[1,*] , **T Kissinger**[1,3] , **S E Staines**[1], **S Prince**[2] ,
E Alcusa-Saez[1,4], **N J Lawson**[2,5] **and R P Tatam**[1]

[1] Centre for Engineering Photonics, Cranfield University, Bedfordshire MK43 0AL, United Kingdom
[2] Centre for Aeronautics, Cranfield University, Bedfordshire MK43 0AL, United Kingdom

E-mail: s.w.james@cranfield.ac.uk

CrossMark

Abstract

Range resolved interferometry (RRI) applied to the interrogation of an extrinsic Fabry–Perot based pressure sensor in laboratory and wind tunnel environments is presented. A simple, compact sensor head design was fabricated and subsequently characterised using RRI, which was shown to have a sensitivity of 1.627×10^{-3} rad Pa^{-1} with a noise standard deviation of 9 Pa over a data rate of 1.5 kHz. When installed in a high-lift wing for surface pressure evaluation during wind tunnel testing, the approach outlined here was able to perform as well as a conventionally employed commercial device for relative static pressure measurements.

Keywords: interferometry, wind tunnel, optical fibre sensors, pressure measurements, high-lift wing, RRI, Fabry–Perot

(Some figures may appear in colour only in the online journal)

1. Introduction

The measurement of pressure is of fundamental importance in the characterisation of aerodynamic structures [1, 2]. In the past decade, optical fibre pressure sensors have received a large amount of interest from the research community. In comparison to other transduction methods that rely on a change in an electrical signal, optical fibre devices are relatively immune to electromagnetic interference, are light-weight and compact in size, and offer the possibility of multiplexing.

The inherent hydrostatic pressure sensitivity of light propagating within an optical fibre is low [3]. In order to enhance this, means of packaging to transduce the pressure into an axial load acting on the fibre have been widely reported. Typically, these schemes have exploited optical fibre Bragg grating (FBG) technology to allow the monitoring of the resultant changes in the fibre's optical length [4]. While the use of FBGs facilitates multiplexing of a serial array of sensors, the sensitivity of such devices, when interrogated using the widely exploited tuneable laser and spectrometer-based approaches, is typically too low to be of use for aerodynamic measurements. Higher sensitivity can be achieved by the interrogation of short, low finesse optical cavities, where the length of the cavity is pressure-sensitive. Such cavities can be formed between the end faces of two optical fibres, or between the end face of an optical fibre and a flexible diaphragm [5].

Interrogation of low finesse cavity-based pressure sensors can be achieved by several methods. Generally, these can be

[3] Now at Institute of Process Measurement and Sensor Technology, Technical University of Ilmenau, PF 100565, 98694 Ilmenau, Germany.
[4] Now at Epic Games, Technopark, Technoparkstrasse 1, 8005 Zurich, Switzerland.
[5] Now at School of Aerospace, Mechanical and Mechatronic Engineering, The University of Sydney, NSW, Australia.
* Author to whom any correspondence should be addressed.

categorised as either white-light, intensity, or phase demodulation schemes. White light interferometry uses either a broadband source or a tunable laser, producing a channelled spectrum upon interrogation of a Fabry–Perot (FP) cavity. Spectral demodulation approaches include wavelength tracking [6], peak-to-peak measurement [7], and Fourier transformation [8]. While these schemes provide relatively simple processing algorithms, and can provide absolute cavity measurements in the case of the latter approach, they typically suffer from poor resolution and limited demodulation bandwidth [9]. The use of cross-correlation in white light interferometry has been shown to improve resolution [10] however the process is computationally heavy and therefore limits demodulation rates.

Intensity based methods typically involve the use of a laser operating at a single wavelength to monitor intensity changes on the linear portion, around the quadrature point, of the optical cavity's sinusoidal transfer function [11], providing a fast [12], cost-effective means of signal demodulation but at the expense of dynamic range and the need for additional feedback routines [13]. These limitations have been overcome using passive and active phase demodulation techniques. Passive schemes rely on the use of multiple lasers that have a quadrature phase shift between each source, allowing two orthogonal signals to be constructed and the phase changes determined trigonometrically [14–16]. Although high sampling rates and an improved dynamic range can be achieved, the cavity length of the FP must be matched to the interrogation sources to ensure quadrature thus restricting the design of the sensor [17].

Active quadrature phase demodulation involves continual manipulation of the interrogation source in order to avoid some of the cavity design restrictions associated with passive phase demodulation. The most widely exploited active phase demodulation for FP cavity interrogation is the phase generated carrier (PGC), scheme as it offers large dynamic range and high linearity [18]. Traditionally in the PGC approach, a high frequency, sinusoidally modulated laser emission wavelength is used to address the FP cavity with the resulting transfer function demodulated with Bessel function analysis coupled with either an arctangent or differential-and-cross-multiplying algorithm [19, 20]. Despite the benefits previously mentioned, the demodulation accuracy of PGC is adversely affected by laser intensity disturbances, phase delays [19] and phase modulation depth [21], additionally, the wavelength modulation frequency dictates the minimum cavity length that can be interrogated.

The ability to assess pressure at multiple regions along a structure is of particular interest to the aerospace industry, where accurate, high frequency (kHz) measurements are necessary for quantifying the aerodynamic performance of structures [22, 23]. Optical fibre FP pressure sensors are an ideal solution to meet these requirements. However, all of the schemes discussed above cannot easily be implemented for demodulating multiple FP cavities, requiring significant investment in optical components (i.e. the need for multiple sources and detectors) or considerable changes in signal processing [24]. The technique of range resolved interferometry (RRI), the approach employed in this work, has been shown previously to be able to demodulate multiplexed interferometric cavities using a single source and detector [25–27]. RRI is a pseudo-heterodyne signal processing approach that measures relative changes in interferometric phase and has been shown to effectively measure the change in optical path length at sub-nanometre resolution [25] and at high data rates (>kHz) [28]. Furthermore, unlike other active phase demodulation techniques, RRI has been shown to produce highly linear results even in the presence of intensity modulation and higher order reflections [25]. However, RRI has not been previously exploited for FP based pressure sensing, therefore the work presented here demonstrates the interrogation of a single external FP pressure sensor using RRI in a wind tunnel. It is shown that accurate, high frequency pressure measurements can be obtained in a wind tunnel using a simple, diaphragm-based optical fibre-based FP sensor head.

The remainder of the paper is outlined as follows. Section 2 describes relevant theory and fabrication of the RRI interrogated FP pressure sensor, as well as the calibration and wind tunnel test schedule. The results from the FP pressure sensor and a widely utilised electrical pressure transducer from the aforementioned experiments are compared and analysed in section 3. This is followed in section 4 by critical analysis of the phase measurement errors and their potential sources in relation to the sensor head. Finally, the outcomes of the research are summarised in section 5.

2. Method

2.1. Operating principle of the FP pressure sensor

FP based pressure sensors require two parallel reflective surfaces to form the cavity. Generally, this is achieved via the use of the cleaved or polished end face of an optical fibre and a diaphragm. This approach provides great flexibility through the choice of diaphragm material, which significantly influences the sensitivity of the sensor and thus the pressure range in which the device will operate [29]. The basic operation of a diaphragm-based FP pressure sensor relies on the relationship between the change in pressure and the resulting change in sensor cavity length caused by the associated diaphragm deflection. If a uniformly distributed load is applied to a circular diaphragm, the following relationship can be used to calculate the expected diaphragm deflection, w, [30],

$$w = \frac{\Delta P r^4}{64D} \left(1 - \frac{a^2}{r^2} \right)^2 \quad (1)$$

where a is the radial location of the deflection point, r is the radius of the diaphragm, and ΔP is the change in pressure. D represents the flexural rigidity and is defined as,

$$D = \frac{Eh^3}{12(1 - v^2)} \quad (2)$$

with E and v being the Young's modulus and Poisson ratio of the diaphragm, respectively, and h is its thickness.

Typically, the arrangement described above is used to form a low finesse FP cavity, where the resulting interference spectrum, I, can be modelled using the general two-beam interference expression [31],

$$I = A + B\cos(\Delta\phi) \tag{3}$$

where A is the average optical intensity, B is the visibility, and $\Delta\phi$ is the phase difference between the two-reflective surfaces and is defined as,

$$\Delta\phi = \frac{4\pi nL}{\lambda_0} \tag{4}$$

where $\Delta\phi$ is dependent on the cavity length, L, and the refractive index of the cavity medium, n, for a given optical vacuum wavelength, λ_0. It is this dependence on L that is exploited by the pressure sensor here, where changes in pressure can be measured via the demodulation of $\Delta\phi$, which, in this case, was achieved using RRI processing techniques outlined in [32].

This approach interrogates one or multiple low-finesse FP cavities via a continuous-wave laser diode that is subject to a sinusoidal modulation of its injection current, which results in a concomitant sinusoidal modulation of the output optical frequency. This yields a return signal that, assuming negligible signal processing delays, is given by [32],

$$I(t) = A + B\cos(A_L\sin(\omega_m(t - 0.5\tau_L)) + \Delta\phi). \tag{5}$$

Here $\omega_m(t)$ is the laser modulation angular frequency, τ_L is the cavity time-of-flight, and A_L is the phase carrier amplitude defined as,

$$A_L = \frac{2\Delta\omega}{\omega_m}\sin\frac{\omega_m\tau_L}{2} \approx \Delta\omega\tau_L \quad \text{for } \tau_L \ll \frac{1}{\omega_m} \tag{6}$$

in which $\Delta\omega$ is the amplitude of the optical frequency modulation of the laser output. The length of the cavity is encoded in this signal via the dependence of the phase carrier amplitude upon the cavity time of flight $\tau_L = 2nL/c$, where c is the speed of light in vacuum.

As this signal is highly chirped, the demodulation approach requires that it is subject to a Gaussian window function that is centred on the quadrature point of the current modulation. Demodulation is achieved by numerically generating a complex carrier,

$$C(t) = \exp(jA_C\sin(\omega_m t)) \tag{7}$$

that possesses phase carrier amplitude, A_C, approximately equal to A_L, which is multiplied by the filtered photodiode signal and then low pass filtered to remove unwanted harmonics of the baseband signal. Analysis of the amplitude of the real and imaginary terms of the output from the low pass filtered signal allow the phase to be determined and subsequently unwrapped. Through use of carriers with different phase carrier amplitudes A_C, signals from multiple constituent interferometers with differing optical path difference (OPD) can be simultaneously demodulated, subject to a minimum OPD difference determined by the amplitude of the wavelength modulation [32].

2.2. Sensor configuration

The minimum cavity length that can be resolved with the RRI approach implemented here is limited to approximately 8 mm by the amplitude of the wavelength modulation achievable via the injection current modulation of the distributed-feedback laser employed. To allow the construction of a compact head, with no auxiliary optical components, the optical cavities to be demodulated were formed between the diaphragm and two in-fibre reflectors. This allowed the tip of the optical fibre to be position in close proximity to the diaphragm. To minimise the influence of parasitic cavities that could not be resolved by the RRI approach, fibre was terminated in an 8° angle polished ferrule, with a corresponding 60 dB suppression of the back reflection. In this configuration, there are three optical cavities of different lengths, formed between each of the in-fibre reflectors (see section 2.3 for details) and the diaphragm, and between the in-fibre reflectors themselves, resulting in the highly-chirped photodiode signal seen in figure 1(b). The dependence of the phase carrier amplitude on the cavity length (equation (6)) allows each of these cavities to be interrogated independently by using complex demodulation carriers with appropriate values of A_L. This can be seen from the plot shown in figure 1(c), where the peaks correspond to each of the defined cavities.

The phases of the cavities formed between R1 and the diaphragm, α, and between R2 and the diaphragm, γ, are influenced by the effects of pressure induced movement of the diaphragm, while the cavity formed between R1 and R2, β, has been included for performance analysis only (used in section 4). The phase data used to derive the pressure measurements here were determined through the interrogation of α only.

Assuming that the diaphragm is formed from aluminium foil of thickness $h = 30\,\mu\text{m}$ and radius $r = 1.25\,\text{mm}$ and with Young's modulus $E = 70 \times 10^9$ and Poisson's ratio $v = 0.35$, and that the illuminating wavelength is $\lambda = 1521\,\text{nm}$, the pressure sensitivity is calculated to be $1.755 \times 10^{-3}\,\text{rad Pa}^{-1}$. Assuming an instrument phase noise floor of $1 \times 10^{-4}\,\text{rad}$ $(\text{Hz}^{1/2})^{-1}$ above 100 Hz [32], which is cavity length independent, the estimated pressure noise floor is $\approx 0.06\,\text{Pa}\,(\text{Hz}^{1/2})^{-1}$.

2.3. Sensor fabrication

As described in previous work that has implemented RRI for optical fibre sensors [27, 33], the in-fibre reflectors, R1 and R2, were realised via the use of ultra-short and low reflectivity FBGs (LRFBGs). The locations of the LRFBGs in relation to the diaphragm were chosen to avoid overlap between desired and parasitic constituent interferometers, and as a result they were separated by 35 mm. Fabrication of the 250 μm long LRFBGs in polyacrylate coated SMF28 optical fibre was performed in a point-by-point fashion via a femtosecond laser operating at a wavelength of 520 nm, with a pulse length of 150 fs and with a repetition rate of approximately 1 kHz (Spirit One, SpectraPhysics) using a micro-optics fabrication system. The length and period of the LRFBGs were selected so the reflection peak had a full-width half maximum of
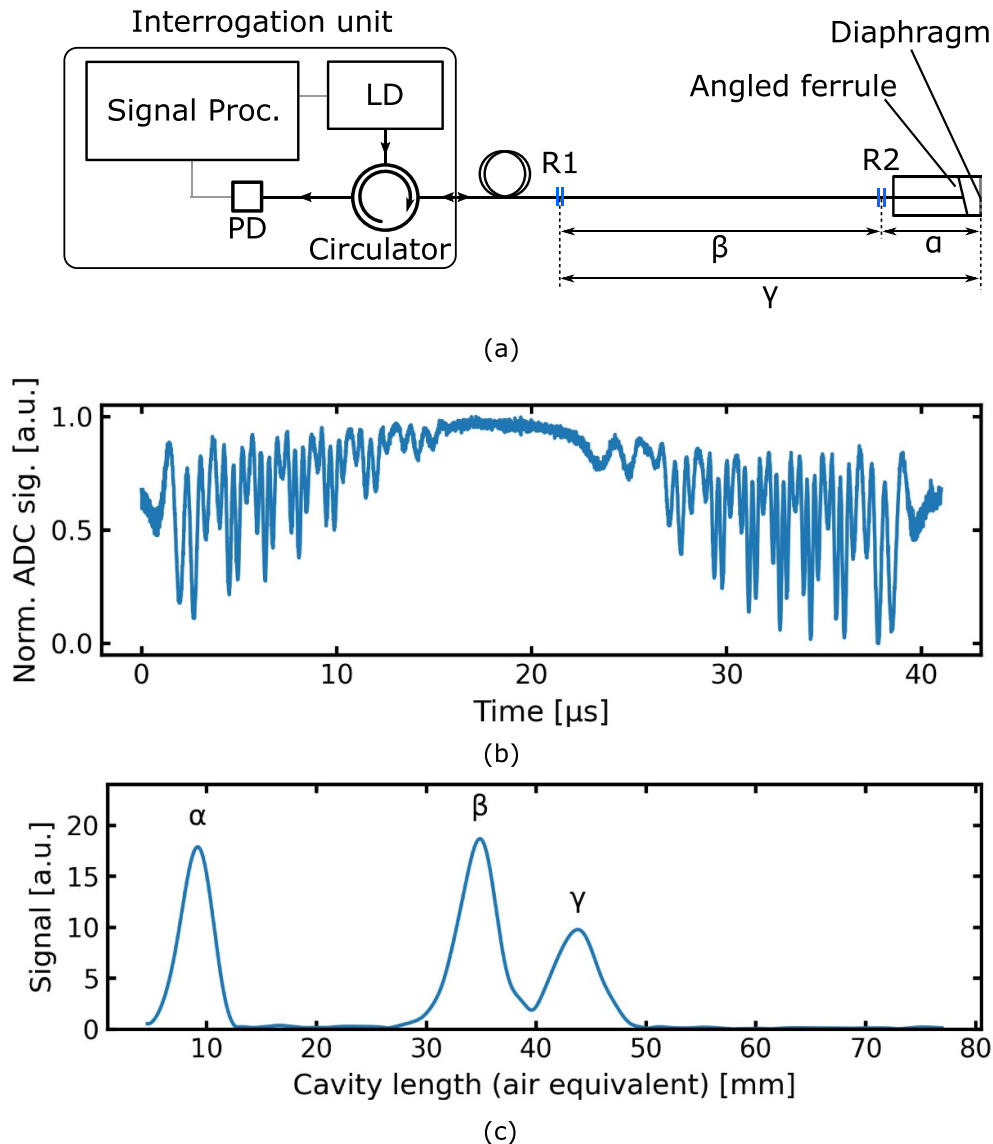
Figure 1. Diagram showing the optical setup with the position of the low reflectivity fibre Bragg grating reflectors (R1 and R2) in relation to the diaphragm of the external FP pressure sensor (a), the full spectrum of the FP sensor from a single laser period (b), and a plot showing the resolved cavities of the FP sensor following RRI signal processing. LD—laser diode; PD—photodiode.

approximately 5 nm with a centre wavelength of 1521 nm and reflectivity of 0.01%. The broad reflection peak ensured that a return signal at the laser wavelength would be observed despite any temperature induced changes in the Bragg wavelength during the experimental test.

The construction of the low-finesse FP static pressure sensor was based on the design reported in [34]. The optical fibre was glued into a castellated cylindrical ceramic ferrule, with a length of 8 mm and diameter of 2.5 mm, using a two-part epoxy adhesive (Araldite), such that R2 (see figure 1(a)) was located 9 mm from the fibre end face. The ceramic ferrule had been polished with an angled end face of 8° in relation to the fibre axis and a D-configured cross section, allowing a stainless-steel capillary tube, with inner and outer diameter of 0.35 and 0.5 mm, respectively, to be adhered to the flat portion of the ferrule to function as an atmospheric reference pressure tap (figure 2(a)).

A circular diaphragm of 3.5 mm diameter was die-stamped from a 30 μm thick aluminium sheet (purity >99%) and attached to a ceramic sleeve of length 8 mm, outer diameter of 3.5 mm, and inner diameter of 2.5 mm, using a cyanoacrylate adhesive (figure 2(b)). The sleeve was gently slid over the prepared ferrule and then adhered in place with the two-part epoxy, sealing the sensor head, with the angle polished end of the fibre and the diaphragm separated by ≈500 μm.

2.4. Instrumentation hardware

The injection current applied to a laser diode (Eblana Photonics, EP1512-DM-B), operating at a central wavelength of 1521 nm with a 1 MHz linewidth, was sinusoidally modulated at a frequency of 24.4 kHz, resulting a sinusoidal modulation of the wavelength of the output wavelength with a modulation amplitude of ±0.30 nm. The laser emission was guided into
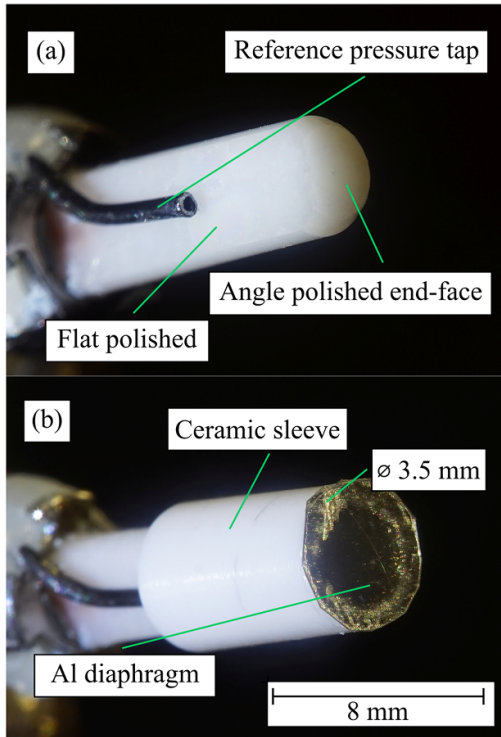
Figure 2. Image of the polished ferrule before (a) and after (b) the mounting of ceramic sleeve with the diaphragm attached.
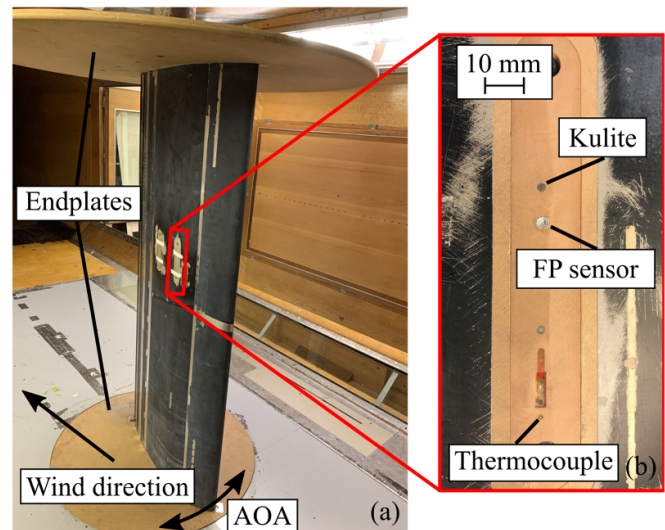

Figure 3. The Helix wing installed in the working section of the 2.4 × 1.8 m wind tunnel (a) with the Necuron sensor block highlighted (b), indicating the FP pressure sensor, Kulite and thermocouple.

the pressure sensor via a single-mode optical fibre circulator, where the returning signal was acquired using an InGaAs photodiode (figure 1(a)). The interferometric signal was then processed with an analogue-to-digital converter and demodulated using field-programmable gate array based signal processing to allow real-time phase acquisition [27]. For short intervals ($\approx$5 s), the interrogation system used could acquire phase measurements at a date rate of 24.4 kHz, however, for the experiments reported here the data was filtered and downsampled on the interrogation unit to a data rate of 1.526 kHz, unless otherwise specified, to allow longer acquisition times (>5 min).

2.5. Sensor installation

The FP pressure sensor was installed in a Necuron block along with a commercial electronic pressure transducer, Kulite XCS-093, to allow the benchmarking of the optical measurements. The Kulite pressure transducer was chosen since it is widely used in wind tunnel tests for aerospace applications [35–37]. The device operates via the use of a fully active, four arm Wheastone bridge that is temperature compensated for operation between -55 °C and 120 °C, and possesses a maximum combined non-linearity and hysteresis of 0.5% of full-scale [38]. The Kulite pressure sensor was calibrated using the protocol outlined in section 2.6 and was determined to have a linear sensitivity of 1.343×10^{-4} V Pa^{-1}. A

K-type thermocouple was also installed alongside the pressure devices (figure 3(b)). The block of sensors was positioned in a recess of the Helix wing (described in detail in section 2.7), 100 mm chordwise from the leading edge and 560 mm spanwise from the top end-plate (see figure 3(a)). The sensor block was installed such that it is long axis was perpendicular to the flow, with the sensors' diaphragms flush with, and normal to, the surface of the wing, thereby ensuring minimal influence of wind directionality. A length of PVC tubing was attached to the atmospheric pressure tap of each pressure sensor to allow the reference pressure to be positioned out of the wind tunnel's free stream. Interrogation of the Kulite sensor was achieved via the use of a high speed DAQ USB X series (National Instruments), with a data acquisition rate of 100 MHz, and a Kulite signal conditioning unit (KSC-2, Kulite) using an in-house written Python script to acquire and process the data. Finally, the K-type thermocouple was monitored using a data logger (USB TC-08, Picolog) and associated software at an acquisition rate of 1 Hz.

2.6. Pressure sensor calibration and characterisation

The FP pressure sensor was calibrated alongside the Kulite under laboratory conditions while the sensor block was installed in the wing. The sensors were exposed to pressures in the range of 4.5 to -4.5 kPa, in steps of 500 Pa, selected based on pressures previously recorded in the wind tunnel at angles of attack (AOA) and wind speeds representative of conditions to be used in subsequent wind tunnel tests (section 2.8). The output from an automated pressure calibration system (Druck PACE5000 with a CM2 control module), with an accuracy of 0.025% of full-scale (3.75 Pa), was attached to the atmospheric reference tubes of the FP and Kulite pressure sensors.

Table 1. Wind tunnel testing schedule and parameter details.

	Operation mode	
	Ramped wind speed	Incremental steps
Wind speed protocol	0 to 40 m s^{-1}, held at 40 m s^{-1} and then returned to 0 m s^{-1}	0 to 40 m s^{-1} in steps of 5 m s^{-1} and held at each wind speed
Angles of attack (°)	10, 12, 14, 16, 18, 20	10, 12, 14, 16, 18, 20
FP acquisition frequency (kHz)	1.526	20
Kulite acquisition frequency (kHz)	1.526	20
Acquisition time (s)	300	10

All measured pressure values obtained were relative to the atmospheric pressure at the start of acquisition. A baffle was placed around the sensors' diaphragms to mitigate any pressure changes caused by air movement created by the laboratory's air handling system. The FP pressure sensor was also characterised for hysteresis. The sensor was initially exposed to −4.5 kPa, increased to 4.5 kPa then returned to −4.5 kPa in increments of 1.0 kPa.

2.7. Wind tunnel and wing model specifications

The facility at Cranfield University is a 2.4 m × 1.8 m (8′ × 6′) general-purpose low speed wind tunnel, which is a closed return system with a 4:1 contraction. The working section provides flow velocities in the range of 5–50 m s^{-1} with a low turbulence level of <0.1% [39].

The tests were conducted using a quasi 2-dimensional, 3-element high-lift wing configuration (Helix), which comprised of a slotted leading edge slat, a main element, and a single slotted trailing edge flap [40]. The model possessed a stowed chord of 0.6 m and a span of 1.4 m. The leading and trailing components were constructed of carbon-fibre and had chords of 0.127 m and 0.18 m, respectively, while the main element was composed of wood. The model spanned 1.4 m between two circular endplates of 1.2 m diameter, to reduce the three dimensionality of the flow over the wing.

2.8. Wind tunnel testing schedule and sensor acquisition details

The Helix wing was installed vertically in the working section of the wind tunnel so that the AOA could be adjusted by rotating the end-plates (figure 3). Optical fibre and electrical leads, in addition to the PVC tubing used for atmospheric referencing, were passed out of the wing through an internal channel and into the control room via the central strut. The test schedule consisted of two operation modes, with the details outlined in table 1. The AOAs were selected to create an unsteady, separated flow around the stall point. All wind speed and AOA conditions were repeated 3 times, with testing taking place over a 3-day period.

3. Results

3.1. Calibration and characterisation

Figure 4 shows the calibration curve from the FP pressure sensor in response to pressure in the range −4.5–4.5 kPa. The average phase was calculated over a 5 s period, typically involving ≈ 7600 data points, during each pressure step and plotted against the pressure applied by the calibration system. Following linear regression analysis, the sensitivity of the FP pressure sensor was found to be 1.627×10^{-3} rad Pa^{-1} at an acquisition rate of 1.526 kHz, which is comparable to the value of 1.755×10^{-3} rad Pa^{-1} predicted in section 2.1. It is suspected that the difference between the measured and predicted sensitivities is due to the manufacturing tolerances in the thickness of the aluminium foil that was used to form the diaphragm.

Figure 5 shows the time series for data recorded by the FP pressure sensor and the Kulite device, following the same incremental pressure ramp as used to calibrate both pressure sensors. It can be seen that, in general, the FP pressure sensor measurements are similar to those provided by the Kulite. Additionally, the change in pressure between each pressure step for both devices shows a rate of change of ≈100 Pa s^{-1}, which is identical to the rate of change applied by the Druck pressure calibration system. Furthermore, when the pressure is maintained at a constant value, both the FP pressure sensor and the Kulite show a 2-standard deviations (2σ) noise level of 9 Pa and 6 Pa, respectively, for a bandwidth of 1.526 kHz.

However, it can also be seen in figure 5 that the Kulite response is more linear than our FP interrogated sensor. This was quantitatively confirmed through linear regression analysis by comparing the Pearson's correlation coefficient, where a value further from 0 (in the range of −1 to −1) shows a stronger linear relationship, which, in this case was 0.9979 for the FP pressure sensor and 0.9999 for the Kulite. The discrepancies between the FP and Kulite pressure sensors are most noticeable at applied pressures of 1.5 kPa and −2.5 kPa, where the FP pressure sensor, shows deviations of −220 and −230 Pa, respectively. These differences are attributed to the sinusoidal modulation that is apparent on the calibration data shown in figure 4, which is discussed further in section 4.

Figure 6 shows the results of a study of the hysteresis of the FP pressure sensor, obtained using the hysteresis protocol outlined in section 2.6. The data shows that there is minimal hysteresis in the RRI pressure sensor, where the greatest deviation of 73 Pa was noted at an applied pressure of −500 Pa, equating to an error of 0.8% of full-scale. A summary of performance characteristics can be seen in table 2.

3.2. Wind tunnel trials

Figure 7 displays the pressure response of the FP and Kulite sensors for a 20° AOA during the ramped wind speed protocol described in section 2.8. The background colourmap indicates the wind speed in the tunnel's working section, where, as can be noted by the colour transition, the speed is continually increased until 40 m s^{-1}, held for approximately 30 s, then
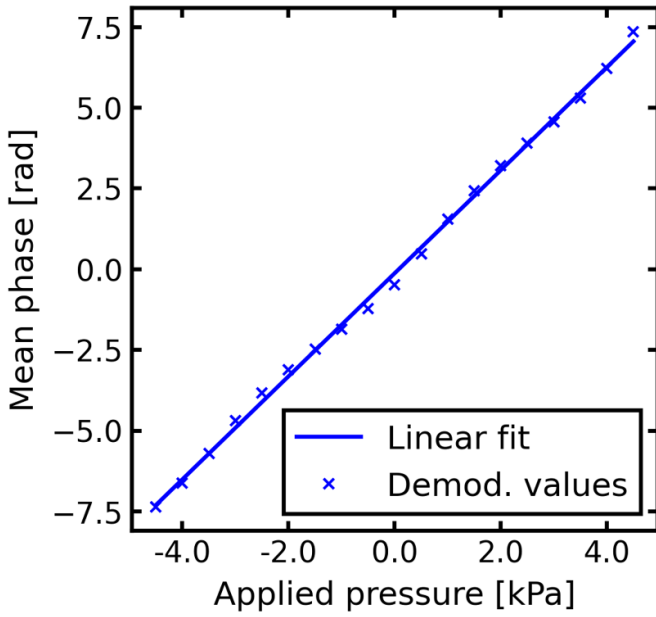
Figure 4. Calibration curve of the FP pressure sensor. Error bars on demodulated values too small to be discerned.
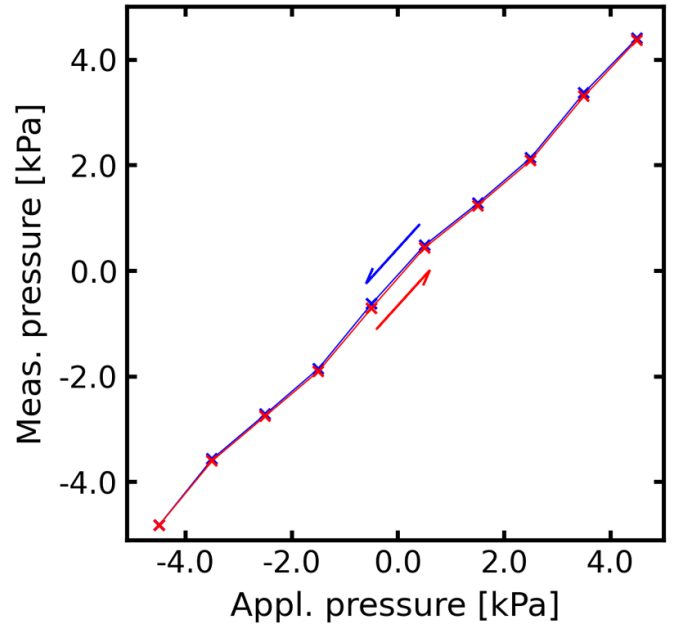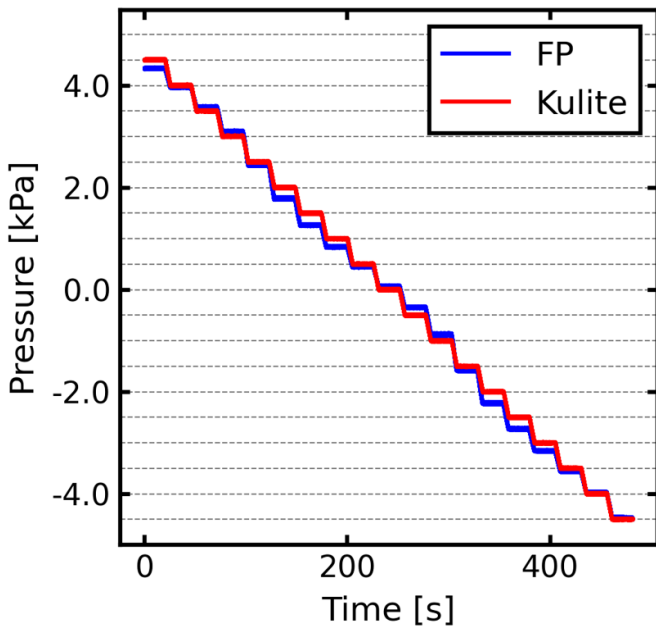

Figure 5. Comparison of recorded pressures between the FP pressure sensor and the Kulite for the basic calibration protocol. Dashed grey lines represent the pressures applied by the automated calibration system.

reduced back to $0\,\mathrm{m\,s^{-1}}$. It can be seen in figure 7 that both sensors displayed a decrease in pressure as the wind speed increased, which since they are positioned on the upper suction surface, is expected. At $40\,\mathrm{m\,s^{-1}}$, the FP sensor showed a similar pressure to that measured by the Kulite, approximately $-4.0\,\mathrm{kPa}$ for a 20° AOA, this is equivalent to a pressure coefficient of -4.154, consistent with previous data for a similar 3-part high-lift aerofoil [41].

Figure 6. The response of the FP pressure sensor following the application of a pressure cycle from $4.5\,\mathrm{kPa}$ to $-4.5\,\mathrm{kPa}$ then returning to $4.5\,\mathrm{kPa}$, where the blue and red arrows indicate decreasing and increasing pressure, respectively.

Table 2. Performance comparison between our FP pressure sensor and Kulite.

	FP	Kulite
Sensitivity ($\times10^{-3}$)	$1.627\,\mathrm{rad\,Pa^{-1}}$	$0.134\,\mathrm{V\,Pa^{-1}}$
Hysteresis (% full-scale)	0.80%	0.50%
2σ noise (Pa)	9	6
Linearity	0.997	0.999

In addition to the agreement of the pressures measured at a wind speed of $40\,\mathrm{m\,s^{-1}}$, the change in pressure measured by both devices as the wind speed was ramped up and down is also similar. However, there is a noticeable difference at $\approx 1.0\,\mathrm{kPa}$ in figure 7, which is thought to be caused by the non-linear response previously mentioned.

Comparing 5 s averaged pressure intervals at $40\,\mathrm{m\,s^{-1}}$ for all tested AOA for both the Kulite and FP pressure sensor (figure 8), it can be seen that as the AOA increases, the pressure on the surface of the wing decreases in both devices. This is to be expected since as the wing pitches up, the airflow acceleration around the leading edge increases resulting in both transducers experiencing higher levels of suction (negative gauge pressure). From figure 8 it can also be seen that the noise is comparable between the Kulite and FP sensor. However, there is a discernible difference in mean pressures between the two devices as the AOA is reduced. Since the ramped tunnel wind speed test schedule started at 20° and then decreased in AOA for subsequent trials, this difference is most likely caused by the ambient temperature in the tunnel increasing as the testing schedule progressed throughout the day. An increase in temperature would be expected to result in an increase in the
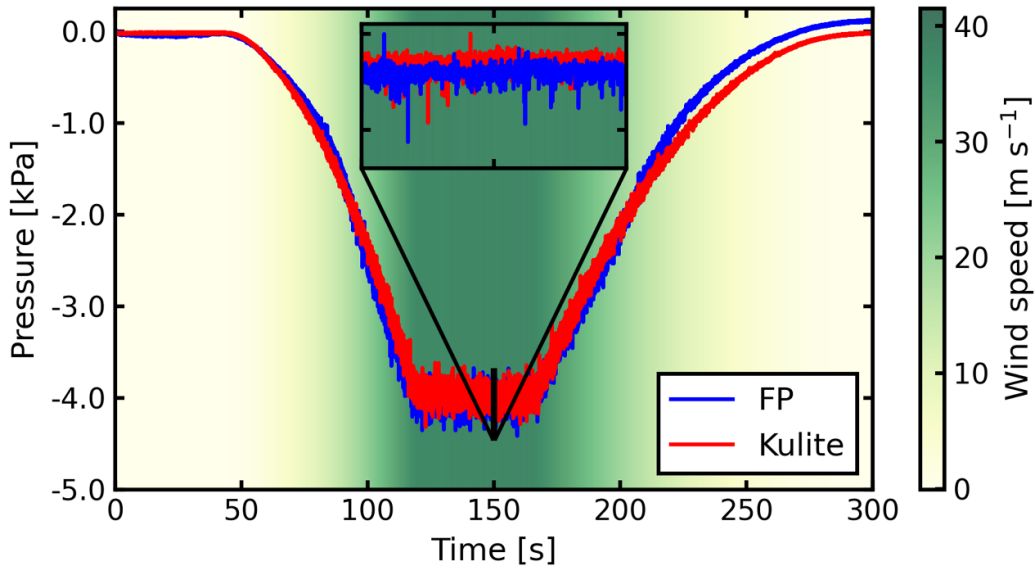
Figure 7. Pressure measurements obtained from both Kulite (blue) and our FP pressure sensor (red) at 1.526 kHz during the ramped wind speed protocol a 20° AOA, where white and dark green on the background colourmap represent wind speeds of 0 m s^{-1} and 40 m s^{-1}, respectively. The inset displays a 1 s interval over a range of 750 Pa.

cavity length due to the thermal expansion of the sensor housing, producing a positive phase shift and yielding a drift in the pressure measurement baseline. While the FP sensor was not thermally calibrated, it was estimated that it has a temperature sensitivity of ≈ 60 Pa °C^{-1}, based on the thermal expansion of zirconia ceramic (the ferrule and sleeve material), as this would be the dominant contributor to a temperature induced cavity length change. Using this thermal sensitivity estimate to compensate for temperature, it can be seen in figure 8 that, for the 2 °C increase noted by the thermocouple between the ramped tests involving AoAs of 10° and 20°, this would reduce the mean pressure of the 10° AOA by ≈ 120 Pa to ≈ -2750 Pa, resulting in a similar difference noted between our FP pressure sensor and the Kulite at an AoA of 20°.

As well as providing relative static pressure measurements comparable to the Kulite sensor, the FP pressure sensor here was also able to discern frequency information. Figure 9 shows a spectrogram derived from short-time Fourier transforms of the pressure measurements during the ramped wind speed protocol at a 20° AOA. Initially, it can be seen that the measurements from both the FP and the Kulite pressure sensors exhibit similar frequency information, where, as the wind speed increases, the intensity of all frequencies increases. This increase in intensity for all frequencies is a result of the increased energy availability in the turbulent boundary layer, derived from the faster tunnel wind speed. It can also be seen in figure 9 that there a number of constant frequencies present in both pressure devices throughout the trial. These are most likely electronic noise signals since they are present when the wind speed was 0 m s^{-1}. It can be seen in figures 9(a) and (b) that at ≈ -4.0 kPa there is a feature present at a frequency of 690 Hz in the data from both the FP pressure sensor and the Kulite. To investigate this, spectral analysis of the data
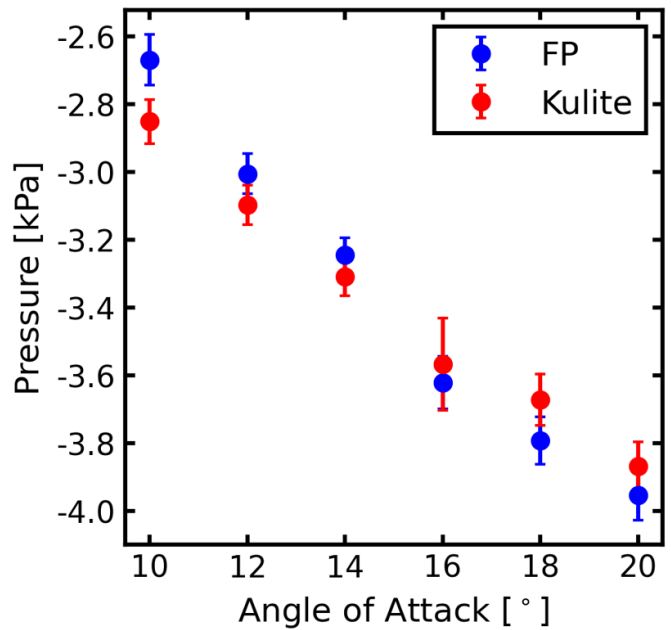

Figure 8. Relationship between average pressure and angle of attack for the RRI pressure sensor and Kulite at 40 m s^{-1}. Error bars represent 2 SD.

obtained during the 10 s steady state runs was undertaken, where the FP and Kulite sensors were acquiring data at rates of 24 kHz and 20 kHz, respectively.

Figures 10(a) and (b) show the amplitude spectral density, determined using Welch's method, for data acquired at wind speeds of 0 m s^{-1} and 40 m s^{-1}. The spectra suggest that the feature at 690 Hz in figures 9(a) and (b) is in fact an aliased frequency from a signal at 900 Hz. Furthermore, the RRI pressure sensor was also able to detect turbulent frequencies features
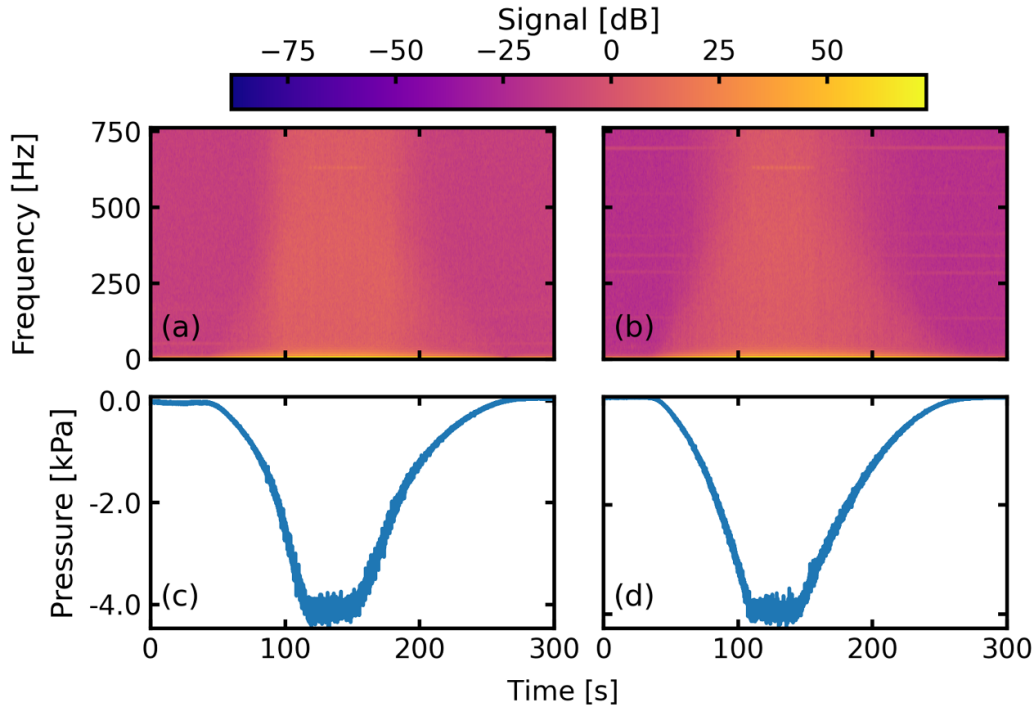
Figure 9. Spectrograms for FP (a) and Kulite (b) pressure sensors during the ramped wind speed protocol at 20° AOA with their associated time series (c) and (d), respectively.
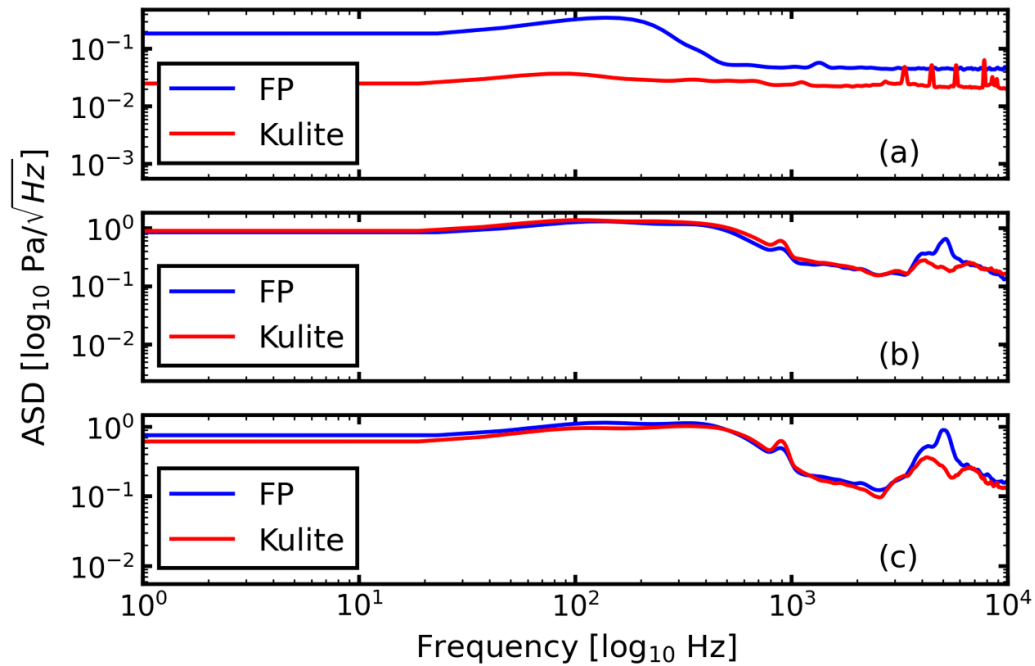

Figure 10. Amplitude spectral density (ASD) determined from the FP and Kulite pressure sensors acquiring at 24 kHz and 20 kHz, respectively, for no wind speed (a) and during the 18° (b) and 20° (c) AOA steady-state runs at a wind speed of 40 m s^{-1}.

around 4 kHz that were also recognised in the Kulite transducer (figures 10(b) and (c)). Although the Kulite possesses a lower noise floor than the RRI interrogated pressure sensor in figure 10(a), the noise is comparable at freestream flow of 40 m s^{-1} for AOAs of 18° and 20° (figures 10(b) and (c)).

Interestingly, it can also be seen that when there is no air movement in the tunnel, the RRI pressure sensor shows lower background electronic noise, where there are multiple frequency signals between 3 and 8 kHz observed only in the Kulite data (figure 10(a)).
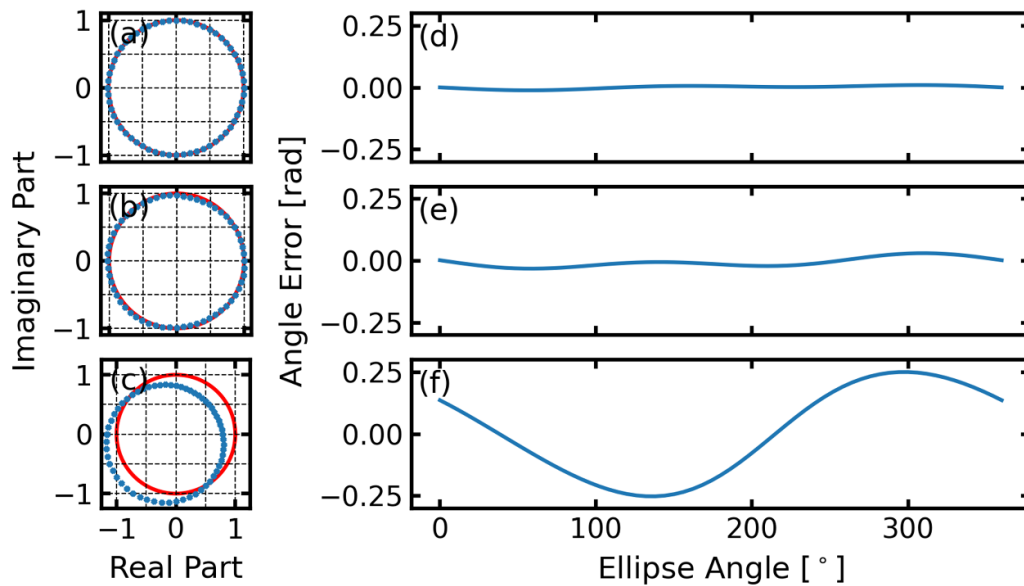
Figure 11. The normalised complex quadrature signal for a 2π phase shift presented in a Lissajous plot for the interferometer β (a) and γ (b) during a localised temperature increase of β, along with γ during the initial pressure decrease of the calibration test (c) (the solid red circle representing the ideal Lissajous figure is numerically generated to aid visualisation). (d), (e), and (f) are the angular error associated with (a), (b), and (c), respectively.

4. Discussion

Whilst the results presented here demonstrate that RRI is a suitable technique for interrogating a FP style pressure sensor, there was a notable modulation seen in the calibration data (figure 4). This modulation clearly has an effect on the accuracy of the pressure measurement and thus the prospects of using this technique in future applications. Since this response possessed a sinusoidal waveform, it is likely that it was derived from cyclic errors associated with the RRI signal processing and therefore it is important to understand the source of this modulation.

A simple test was conducted that involved gently heating the interferometer formed between reflectors R1 and R2 (β, see figure 1) from 20 °C to 50 °C and assessing the resulting complex signal from cavities β and γ (R1 and the diaphragm) over a period of 2π when plotted as a Lissajous diagram. A non-circular and non-centred form, would indicate the presence of cyclic errors [42, 43]. These results were compared to a Lissajous plot generated from the pressure calibration data, also over a 2π interval. The Lissajous plots were generated by averaging the quadrature amplitudes over 30 angular sectors and plotting them in the complex plane. Quantification of the angular errors were established through the application of a Heydemann ellipse to the averaged sectors [44]. Figures 11(a), (b), (d) and (e) show that, when interrogating the cavities β and γ during a localised temperature increase, the cyclic errors are minimal, equating to an angular error magnitude of 0.010 and 0.030 rad, respectively, where the slight increase in error in the latter appears to derive from the static diaphragm. However, as is depicted in figures 11(c) and (f), when the diaphragm is deflected due to pressure variations, the data in the complex plane is clearly off-centre and

the angular error is significantly increased to a magnitude of 0.250 rad. When compared to the residuals calculated from the linear regression analysis used to generate the calibration curve for the RRI pressure sensor (figure 4), the errors depicted in figure 11(f) are of a similar magnitude.

The data presented in figure 11 demonstrates that the bulk of the cyclic errors are introduced by the design of the sensor head and are not inherent to the RRI signal processing. It is suspected that the large offset from the centre seen in figure 11(c) derives from demodulation of the overlap of two cavities, namely, γ and a cavity between R1 and the angle-polished fibre tip (see figure 1). Since both of these cavities share similar optical path lengths which cannot be resolved by the RRI processing, it is not possible to demodulate them separately using this current setup, thus the phasors from each cavity are processed as one. During the localised temperature increase, the issue seen in figure 11(c) is masked because the two cavities are changed to an equal degree since the phase signals are dominated by the common temperature-induced phase change between R1 and the fibre tip for both cases. Therefore, their respective phasors rotate together and minimum cyclic errors are observed. However, during a pressure change, only the length of γ is dependent on the diaphragm and thus the phasor associated with this cavity rotates around the static phasor relating to the R1-angle-polished ferrule cavity. Although the ferrule was angle polished to strongly suppress back reflections, it is clear from figures 11(c) and (f) that the signal strength from the angle polished ferrule was of significant, non-negligible magnitude compared to the returning signal from the diaphragm. Therefore, in order to significantly reduce the cyclic errors seen here, a change in sensor head design would be required either through increasing the cavity length between the ferrule and diaphragm such that the

cavity could be demodulated using RRI (>8 mm), further suppress back reflections by either increasing the polished angle on the ferrule (>8°) or applying an anti-reflective coating to it, or by significantly increasing the signal from the diaphragm thereby causing the signal contribution from the ferrule to be negligible.

A direct comparison of the pressure sensing performance stated here with previously published literature is difficult due to the pressure sensitivity dependence of differing diaphragm materials. However, when comparing phase noise with other active phase demodulation techniques such as PGC, the technique proposed here is of a comparable level [19]. Furthermore, the use of RRI as signal processing technique for low-finesse FP sensors reduces the constraints on sensor design when compared to PGC. The demodulation algorithm of PGC requires the carrier modulation depth (CMD), which is dependent on cavity length and the maximum frequency shift of the laser [45], to be an optimal value in order to ensure minimal harmonic distortion [9]. This dependence of CMD on cavity length means that sensor heads and modulation parameters have to be specifically tuned to take this into consideration. However, the demodulation approach that underpins RRI allows the interrogation of any cavity length that is greater than a minimum OPD, determined by the frequency modulation excursion (see section 2.1), and can provide highly linear measurements with no requirement to balance cavity length, optical frequency modulation depth and operating wavelength, thereby significantly easing sensor head design restrictions.

5. Conclusion

The work presented here has described the novel use of RRI to interrogate a fibre optic FP pressure sensor, with the contribution being the demonstration of an optical sensor with measurement performance equivalent to that of an industry standard electrical pressure sensor used for aerodynamically relevant measurements in relative static pressure and frequency analysis on a high lift wing in a wind tunnel. The sensitivity of the sensor was determined to be 1.627×10^{-3} rad Pa^{-1} with a noise floor of 9 Pa over a bandwidth of 1.526 kHz during steady state characterisation. The operation of the device in a harsh environment such as the wind tunnel indicates that this approach is robust for exploitation in other challenging aerospace and industrial applications, with the measurement characteristics tailored by appropriate selection of diaphragm material thickness and diameter. Future work will investigate the use of different sensor head designs to compensate for the influence of temperature and reduce the effects of cyclic errors, in addition to exploiting the principles of RRI to facilitate multiplexed optical fibre pressure sensing.

Data availability statement

The data that support the findings of this study are openly available at the following URL/DOI: 10.17862/cranfield.rd. 21444807.

ORCID iDs

J H Barrington ⬤ https://orcid.org/0000-0002-1177-5616
S W James ⬤ https://orcid.org/0000-0003-0651-9842
T Kissinger ⬤ https://orcid.org/0000-0003-1832-7143
S Prince ⬤ https://orcid.org/0000-0002-5545-3344
N J Lawson ⬤ https://orcid.org/0000-0002-1915-8209
R P Tatam ⬤ https://orcid.org/0000-0001-9599-3639

References

[1] Ukeiley L and Murray N 2005 Velocity and surface pressure measurements in an open cavity *Exp. Fluids* **38** 656–71
[2] Gao Y, Zhu Q and Wang L 2016 Measurement of unsteady transition on a pitching airfoil using dynamic pressure sensors *J. Mech. Sci. Technol.* **30** 4571–8
[3] Xu M, Reekie L, Chow Y and Dakin J P 1993 Optical in-fibre grating high pressure sensor *Electron. Lett.* **29** 398–9
[4] Correia R, Chehura E, James S W and Tatam R P 2007 A pressure sensor based upon the transverse loading of a sub-section of an optical fibre Bragg grating *Meas. Sci. Technol.* **18** 3103–10
[5] Yu Q and Zhou X 2011 Pressure sensor based on the fiber-optic extrinsic Fabry–Perot interferometer *Photonic Sens.* **1** 72–83
[6] Correia R, Staines S E, James S W, Lawson N, Garry K and Tatam R P 2014 Wind tunnel unsteady pressure measurements using a differential optical fiber Fabry-Perot pressure sensor *23rd Int. Conf. on Optical Fibre Sensors (Int. Society for Optics and Photonics)* vol 9157 p 915709
[7] Jiang Y and Ding W 2011 Recent developments in fiber optic spectral white-light interferometry *Photonic Sens.* **1** 62–71
[8] Jiang Y 2008 Fourier transform white-light interferometry for the measurement of fiber-optic extrinsic Fabry–Perot interferometric sensors *IEEE Photonics Technol. Lett.* **20** 75–77
[9] Liu Q and Peng W 2021 Fast interrogation of dynamic low-finesse Fabry–Perot interferometers: a review *Microw. Opt. Technol. Lett.* **63** 2279–91
[10] Wang Z, Jiang Y, Ding W and Gao R 2013 A cross-correlation based fiber optic white-light interferometry with wavelet transform denoising *Fourth Asia Pacific Optical Sensors Conf.* vol 8924 p 89241
[11] Chen J, Chen D, Geng J, li J, Cai H and Fang Z 2008 Stabilization of optical Fabry–Perot sensor by active feedback control of diode laser *Sens. Actuators* A **148** 376–80
[12] Wu N, Zou X, Tian Y, Fitek J, Maffeo M, Niezrecki C, Chen J and Wang X 2012 An ultra-fast fiber optic pressure sensor for blast event measurements *Meas. Sci. Technol.* **23** 055102

[13] Wang Q and Ma Z 2013 Feedback-stabilized interrogation technique for optical Fabry–Perot acoustic sensor using a tunable fiber laser *Opt. Laser Technol.* **51** 43–46

[14] Ezbiri A and Tatam R 1996 Interrogation of low finesse optical fibre Fabry–Perot interferometers using a four wavelength technique *Meas. Sci. Technol.* **7** 117

[15] Ezbiri A and Tatam R 1997 Five wavelength interrogation technique for miniature fibre optic Fabry–Perot sensors *Opt. Commun.* **133** 62–66

[16] Liao H, Lu P, Liu L, Wang S, Ni W, Fu X, Liu D and Zhang J 2017 Phase demodulation of short-cavity Fabry–Perot interferometric acoustic sensors with two wavelengths *IEEE Photon. J.* **9** 1–9

[17] Jia J, Jiang Y, Gao H, Zhang L and Jiang Y 2019 Three-wavelength passive demodulation technique for the interrogation of EFPI sensors with arbitrary cavity length *Opt. Express* **27** 8890–9

[18] Dandridge A, Tveten A B and Giallorenzi T G 1982 Homodyne demodulation scheme for fiber optic sensors using phase generated carrier *IEEE Trans. Microw. Theory Tech.* **30** 1635–41

[19] Zhang A and Zhang S 2016 High stability fiber-optics sensors with an improved PGC demodulation algorithm *IEEE Sens. J.* **16** 7681–4

[20] Liu B, Lin J, Liu H, Ma Y, Yan L and Jin P 2017 Diaphragm based long cavity Fabry–Perot fiber acoustic sensor using phase generated carrier *Opt. Commun.* **382** 514–8

[21] Hou C, Zhang J, Yuan Y, Yang J and Yuan L 2021 Reliability demodulation algorithm design for phase generated carrier signal *IEEE Trans. Reliab.* **71** 127–38

[22] Wang H, Jiang X, Chao Y, Li Q, Li M, Zheng W and Chen T 2019 Effects of leading edge slat on flow separation and aerodynamic performance of wind turbine *Energy* **182** 988–98

[23] D'Alessandro V, Clementi G, Giammichele L and Ricci R 2019 Assessment of the dimples as passive boundary layer control technique for laminar airfoils operating at wind turbine blades root region typical Reynolds numbers *Energy* **170** 102–11

[24] Kirkendall C K and Dandridge A 2004 Overview of high performance fibre-optic sensing *J. Phys. D: Appl. Phys.* **37** R197–216

[25] Wiseman K B, Kissinger T and Tatam R P 2021 Three-dimensional interferometric stage encoder using a single access port *Opt. Lasers Eng.* **137** 106342

[26] Kissinger T, Correia R, Charrett T O H, James S W and Tatam R P 2016 Fiber segment interferometry for dynamic strain measurements *J. Lightwave Technol.* **34** 4620–6

[27] Kissinger T, Chehura E, Staines S E, James S W and Tatam R P 2018 Dynamic fiber-optic shape sensing using fiber segment interferometry *J. Lightwave Technol.* **36** 917–25

[28] Kissinger T, Charrett T O, James S W, Adams A, Twin A and Tatam R P 2016 Characterisation of a cryostat using simultaneous, single-beam multiple-surface laser vibrometry *AIP Conf. Proc.* vol 1740 p 100004

[29] Wang X, Li B, Russo O L, Roman H T, Chin K K and Farmer K R 2006 Diaphragm design guidelines and an optical pressure sensor based on MEMS technique *Microelectron. J.* **37** 50–56

[30] Reddy J N 2007 *Theory and Analysis of Elastic Plates and Shells* 2nd edn (London: CRC Press)

[31] MacPherson W N, Kidd S R, Barton J S and Jones J D C 1997 Phase demodulation in optical fibre Fabry–Perot sensors with inexact phase steps *IEE Proc. Optoelectron.* **144** 130–3

[32] Kissinger T, Charrett T O H and Tatam R P 2015 Range-resolved interferometric signal processing using sinusoidal optical frequency modulation *Opt. Express* **23** 9415–31

[33] Weber S *et al* 2021 Application of fibre optic sensing systems to measure rotor blade structural dynamics *Mech. Syst. Signal Process.* **158** 107758

[34] Lawson N J, Correia R, James S W, Partridge M, Staines S E, Gautrey J E, Garry K P, Holt J C and Tatam R P 2016 Development and application of optical fibre strain and pressure sensors for in-flight measurements *Meas. Sci. Technol.* **27** 104001

[35] Parthasarathy A and Saxton-Fox T 2022 A novel experimental facility to impose unsteady pressure gradients on turbulent boundary layers *Exp. Fluids* **63** 107

[36] Kaczyński P, Szwaba R, Piotrowicz M, Flaszyński P and Doerffer P 2022 Wind tunnel investigations of aircraft airfoil in cruise conditions *J. Phys.: Conf. Ser.* **2367** 012019

[37] Stegmüller J, Katzenmeier L and Breitsamter C 2022 Horizontal tail buffeting characteristics at wing vortex flow impact *CEAS Aeronaut. J.* **13** 779–96

[38] Kulite Product specifications of xcs-093 (available at: https://kulite.com/products/product-advisor/product-catalog/high-sensitivityminiature-pressure-transducer-xcs-093/) (Accessed 9 February 2023)

[39] Cranfield University 8 × 6 wind tunnel (available at: www.cranfield.ac.uk/facilities/8x6-wind-tunnel) (Accessed 13 January 2022)

[40] Knepper A and Garry K 2005 A preliminary investigation of trailing edge serrations in high lift systems *35th AIAA Fluid Dynamics Conf. and Exhibit* p 5261

[41] Wild J 2013 Mach and Reynolds number dependencies of the stall behavior of high-lift wing-sections *J. Aircr.* **50** 1202–16

[42] McRae T G, Hsu M T, Freund C H, Shaddock D A, Herrmann J and Gray M B 2012 Linearization and minimization of cyclic error with heterodyne laser interferometry *Opt. Lett.* **37** 2448–50

[43] Kimbrough B 2014 Correction of errors in polarization based dynamic phase shifting interferometers *Int. J. Optomechatronics* **8** 304–12

[44] Heydemann P L 1981 Determination and correction of quadrature fringe measurement errors in interferometers *Appl. Opt.* **20** 3382–4

[45] Mao X, Tian X, Zhou X and Yu Q 2015 Characteristics of a fiber-optical Fabry–Perot interferometric acoustic sensor based on an improved phase-generated carrier-demodulation mechanism *Opt. Eng., Bellingham* **54** 046107